

SUPPLEMENTARY NOTE

Data Acquisition Methods

Datasets used in this study were collected during the following expeditions: the 33rd and 34th Chinese National Antarctic Research Expedition (CHINARE) (2016/17 and 2017/18), and the 10th International Collaborative Exploration of the Cryosphere through Airborne Profiling program (ICECAP) (AAD/UTIG ICP10, 2018/19). Over the LSE area, most survey profiles are aligned perpendicularly to the main axis of the lake, with a spacing of 15 kilometers (Supplementary Figure 1). Survey lines were flown between 500 and 1000 meters above the ice surface at an average speed of about 90 m/s.

The survey platforms are equipped with the High Capacity Airborne Radar Sounder (HiCARS) developed by UTIG (Greenbaum et al., 2015; Cui et al., 2018), a 60 MHz phase coherent IPR system that provides a depth resolution of about 10 meters in air and about 5.6 meters in ice (Cui et al., 2018). The subglacial hydraulic slope is calculated following the similar procedures as described in Carter et. al. (2007). The tolerance for subglacial hydraulic flatness is set to be 0.2°, as the repeatability statistics of measured bed elevation (29m) and surface elevation (8m) translate into a subglacial hydraulic slope of about 0.2°. The relative basal reflectivity is derived by applying corrections for geometrical spreading and attenuation losses, and normalized around the mean of the measured radar bed echo strength in the surveyed region (Schroeder et al., 2016) (Supplementary Note, Supplementary Figure 12). The process of calculating basal specularity content follows procedures similar to those described in Schroeder et. al. (2015).

The gravity field was measured by a GT-2A airborne gravimeter. The gravimeter is mounted inside the airplane cabin near the aircraft's center of gravity. Gravity data is averaged along track with a 100 second moving window. Gravity reduction used the Gravimetric Technologies

GTGRAV tool, using Precise Point Positioning (PPP) GPS trajectories calculated using Novatel's Waypoint Software. The root mean square (RMS) of the crossover differences in the measured free air gravity anomaly is about 2.1 mGal. The regional trend was then removed using Geosoft Oasis Montaj software package, to eliminate the signal from deeper geological structures. The complete Bouguer gravity anomaly is calculated using the Geosoft Oasis Montaj software package and the Geosoft AirGrav extension.

For the CHINARE aircraft, a CS-3 Cesium vapor magnetometer was used to measure the magnetic field, while a G-823 magnetometer was used on the AAD-operated aircraft. Each magnetometer is mounted on the airplane tail to minimize the interference caused by the metal airframe. Magnetics data was corrected using static data acquired at Zhongshan Station and Davis Station. Over the lake area, the RMS of the crossover differences in magnetic anomaly is about 17.3 nT. The large-scale geomagnetic reference field was removed, and the result was then levelled using Geosoft Oasis Montaj software package.

The maps in Fig. 1B-F and Fig. 3 are interpolated from survey transects using Geosoft Oasis Montaj software package, implementing the minimal curvature method. The geophysical modelling was performed with the Geosoft Oasis Montaj software package and the Geosoft GMSYS extension, implementing the Talwani method (Talwani et al., 1959). We derive the shoreline of LSE from the subglacial hydraulic head, relative basal reflectivity, basal specularity and free-air gravity anomaly (Figure 1, Supplementary Figure 2-6).

Estimation of Average Radar Attenuation Rate

To account for the radar attenuation loss within the ice sheet, we use the minimum correlation coefficient magnitude method (Schroeder et al., 2016) to estimate a global attenuation rate for the LSE dataset (Supplementary Figure 12). When calculating the coefficient magnitude,

we exclude data where the ice thickness is below 1600 meters or greater than 2800 meters, to fulfill the assumption that spatial variations in bed properties and temperature and attenuation rate within the ice sheet are small. The resulting one-way attenuation rate is about 7.55 dB per kilometer, and the uncertainty for this attenuation rate is estimated to be about 1.25 dB/km. This rate represents the column-average of attenuation and is then used to compensate then attenuation loss when calculating the relative basal reflectivity.

Modelling Approach

To constrain the crustal framework of LSE, we calculated the magnetic response for a series of simplified crustal framework models for three transects cross the lake. We then compared the model responses to the measured magnetics anomaly (Supplementary Figure 7-8). Without prior knowledge of the geological conditions in the LSE region, we built the models with two relatively simple geological setting – (1) a magnetized basement and a non-magnetized cap layer, and (2) two magnetized strata within a non-magnetized bedrock. Ice surface elevation and bed topography in the models are derived from IPR sounding. Our modelling results show that the models with compressional geologic features (such as folds and thrust faults) provide a more coherent crustal framework and a better match, which suggests that LSE is located along a compressional geologic boundary. After we establish that LSE is located along a compressional geological boundary, we estimate the locations of the associated thrust faults as follows. The intersection points of the survey transects and the fault's strike are obtained from the magnetic models, and the line of strike is estimated to be perpendicular to the magnetic gradient, assuming the observed magnetic anomaly is predominantly cause by the thrust fault.

To establish a bathymetry model for the LSE area, we built 2-D geophysical inversion models for four different hypotheses: (1): no sediment at the lake bottom with lake bank slopes

projected from surrounding bed rock; (2): sediment layer present at the lake bottom with lake bank slopes projected from surrounding bed rock; (3): no sediments at the lake bottom, while water thickness is constrained by gravity response; (4): sediment layer present at the lake bottom, while water and sediment layer thickness is constrained by gravity response (Supplementary Figure 9). We assume a homogeneous density for the bedrock across the study area. Our geophysical modelling results suggest that the bedrock density value of about 2680 kg/m^3 fits the gravity anomaly curve the best. When comparing the calculated and measured gravity and magnetic anomalies and using the depth to magnetic basement solutions to guide the model selection (Greenbaum et al., 2015), model (4) provides a better match. Additionally, gravity models without sediment result in a water thickness up to over 400 meters (Supplementary Figure 10). We compare this value to the subglacial Lake Vostok. As a reference, the maximum water thickness of the subglacial Lake Vostok is about 1100m, as estimated by Filina et al., 2008, so 400 m is not impossible. However, as Lake Vostok is about 33 times larger than LSE (Lake Vostok is about 12500 km^2 , while LSE is about 370 km^2 in area), we argue that this new water thickness would be unlikely. In addition, Filina et al., 2008 showed that although there was little radar evidence for sediments along the shoreline of Lake Vostok, which is presumed to be dominantly igneous/metamorphic, the bathymetry of the lake excluding a sediment unit was too deep to support the observed lake circulation system (i.e., the distribution of melting and freezing). To support this conclusion, they used sparse but independent seismic indications of sediments beneath the center of the lake in their potential field inversions. In a similar manner, we use the independent indications of sediments along the LSE shoreline to conclude that depths up to 400 m from sediment free models exceed reasonable values. Therefore, based on the

geophysical models and the independent radar observations along the shoreline, we make the argument that unconsolidated sediment exists around and at the bottom of LSE.

We then constrained the lake bathymetry and sediment distribution from the free air gravity anomaly based on this bathymetry model. Uncertainties of the modelled subsurface depth were estimated by comparing a series of models that generate misfit no larger than the repeatability statistics of the measured data. Additionally, we built gravity models with a range of bedrock densities between 2600 kg/m³ and 2900 kg/m³ to constrain the depth context of the water and sediment thickness, as shown in Supplementary Figure 11. The resulting maximum water depth ranges between 200 meters and 400 meters.

REFERENCES CITED:

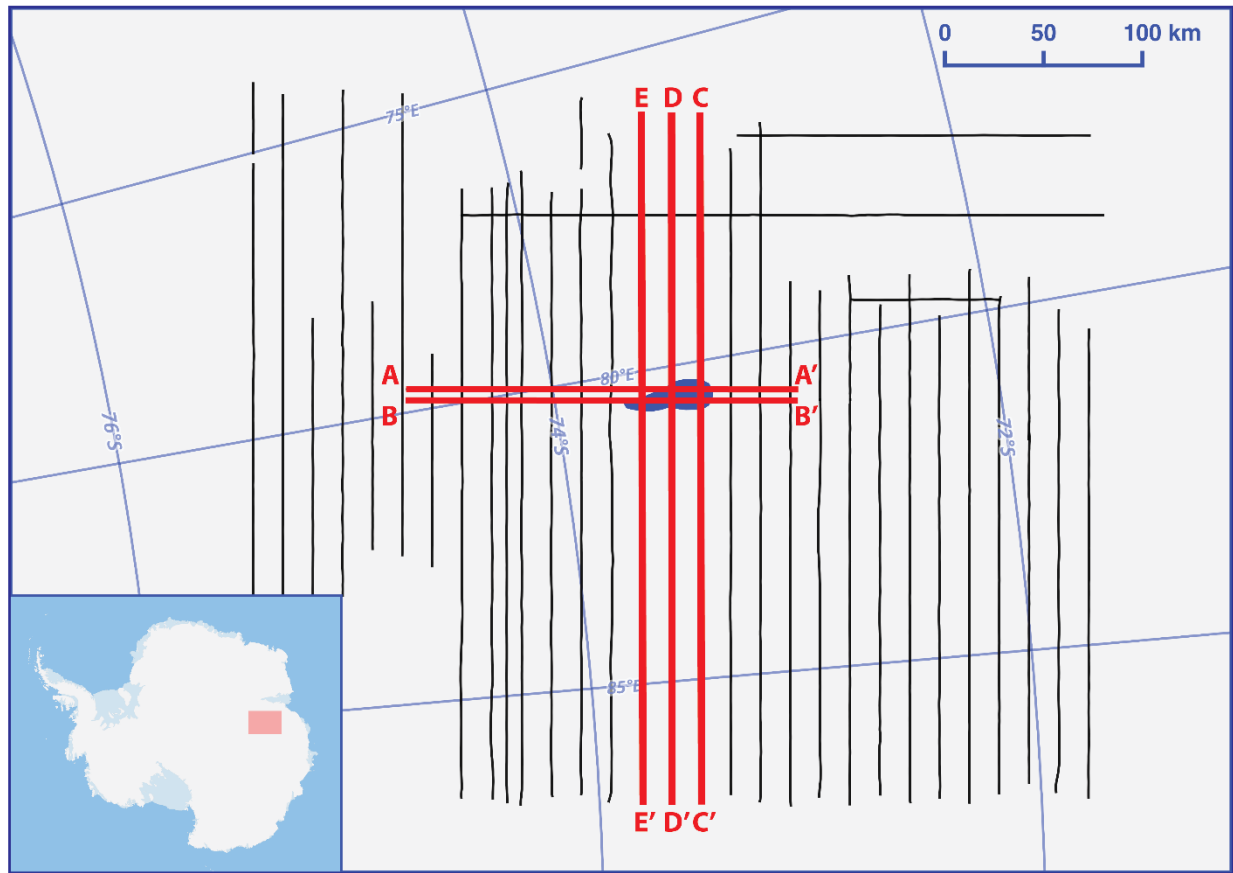
- Carter, S.P., Blankenship, D.D., Peters, M.E., Young, D.A., Holt, J.W., and Morse, D.L., 2007, Radar-based subglacial lake classification in Antarctica: Geochemistry, Geophysics, Geosystems, v. 8, doi:10.1029/2006GC001408.
- Cui, X., Greenbaum, J.S., Beem, L.H., Guo, J., Ng, G., Li, L., Blankenship, D., and Sun, B., 2018, The First Fixed-wing Aircraft for Chinese Antarctic Expeditions: Airframe, modifications, Scientific Instrumentation and Applications: Journal of Environmental and Engineering Geophysics, v. 23, p. 1–13, doi:10.2113/JEEG23.1.1.
- Filina, I.Y., Blankenship, D.D., Thoma, M., Lukin, V. V., Masolov, V.N., and Sen, M.K., 2008, New 3D bathymetry and sediment distribution in Lake Vostok: Implication for pre-glacial origin and numerical modeling of the internal processes within the lake: Earth and Planetary Science Letters, v. 276, p. 106–114, doi:10.1016/j.epsl.2008.09.012.

Greenbaum, J.S. et al., 2015, Ocean access to a cavity beneath Totten Glacier in East Antarctica: Nature Geoscience, v. 8, p. 294–298, doi:10.1038/ngeo2388.

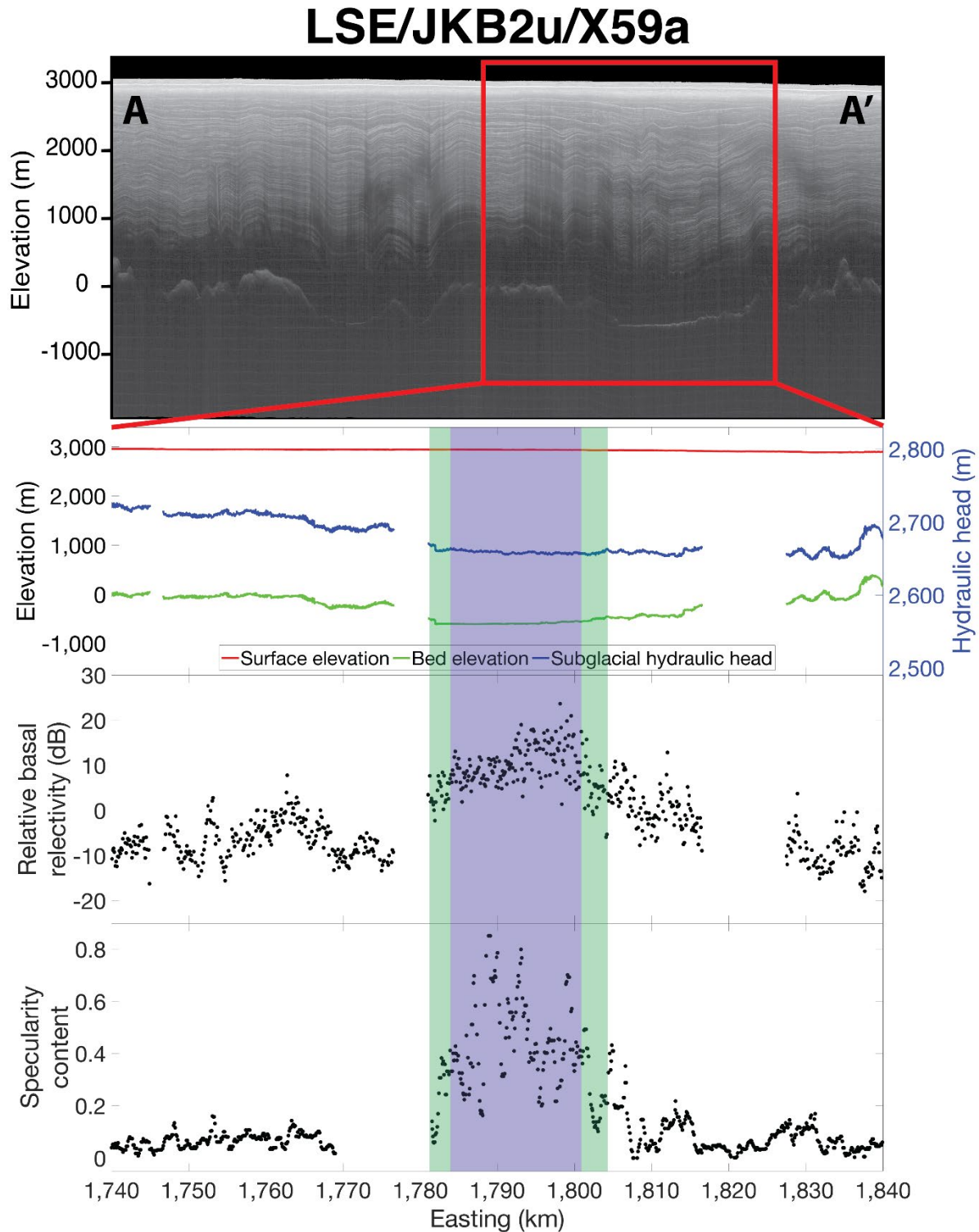
Schroeder, D.M., Blankenship, D.D., Raney, R.K., and Grima, C., 2015, Estimating subglacial water geometry using radar bed echo specularity: Application to Thwaites Glacier, West Antarctica: IEEE Geoscience and Remote Sensing Letters, v. 12, p. 443–447, doi:10.1109/LGRS.2014.2337878.

Schroeder, D.M., Seroussi, H., Chu, W., and Young, D.A., 2016, Adaptively constraining radar attenuation and temperature across the Thwaites Glacier catchment using bed echoes: Journal of Glaciology, v. 62, p. 1075–1082, doi:10.1017/jog.2016.100.

Talwani, M., Worzel, J.L., and Landisman, M., 1959, Rapid Gravity Computations for Two-Dimensional Bodies with Application to the Mendocino Submarine Fracture Zone: Journal of Geophysical Research, v. 64.

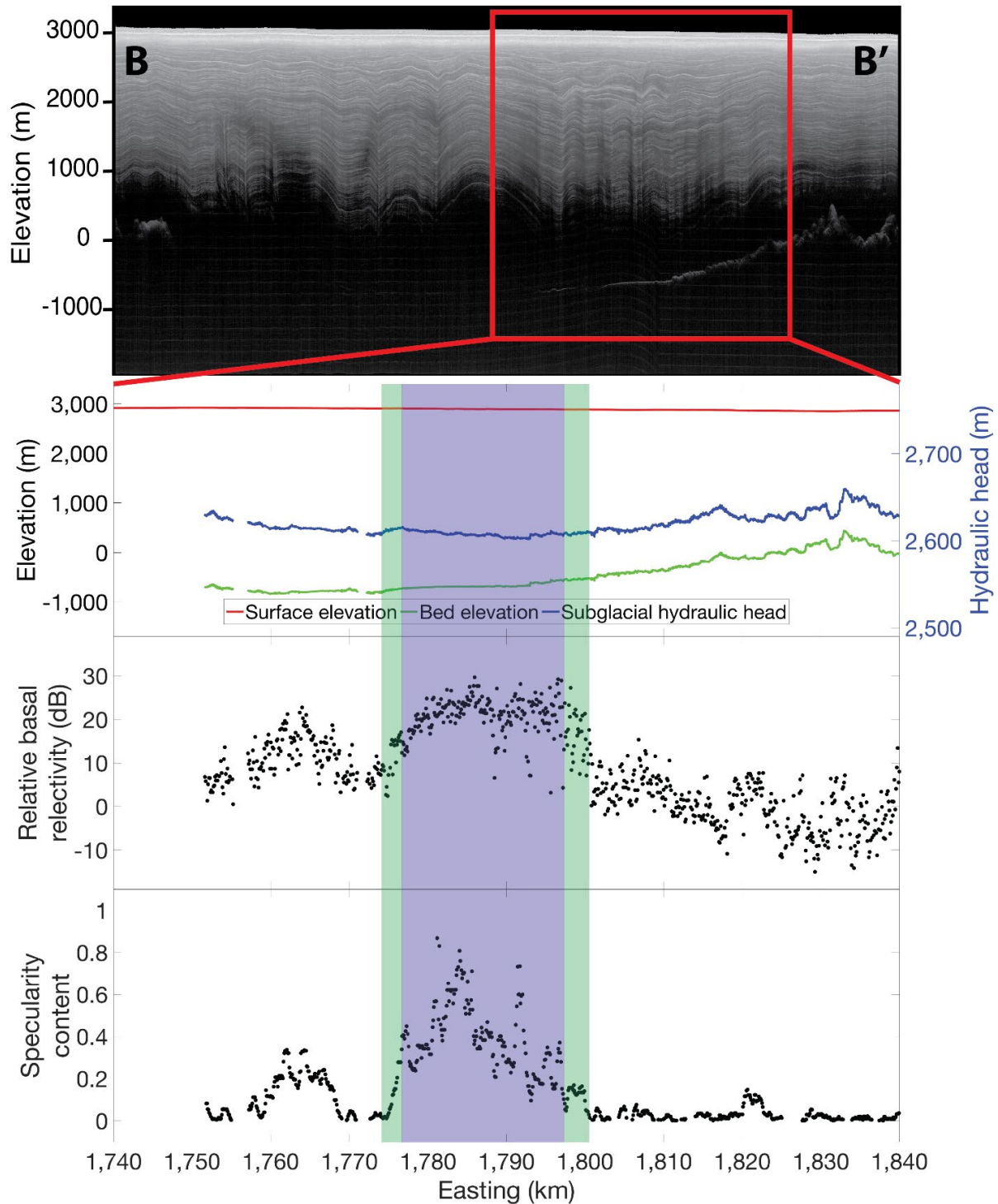


Supplementary Figure 1. Data coverage of the LSE data set. Black lines: aero-geophysics survey transects in the LSE region collected during field seasons CHINARE 33rd and 34th (2016/17 and 2017/18), and AAD/UTIG ICP10 (2018/19). Blue area: location of the subglacial Lake Snow Eagle. Profiles shown in the following figures are highlighted and labelled in red.



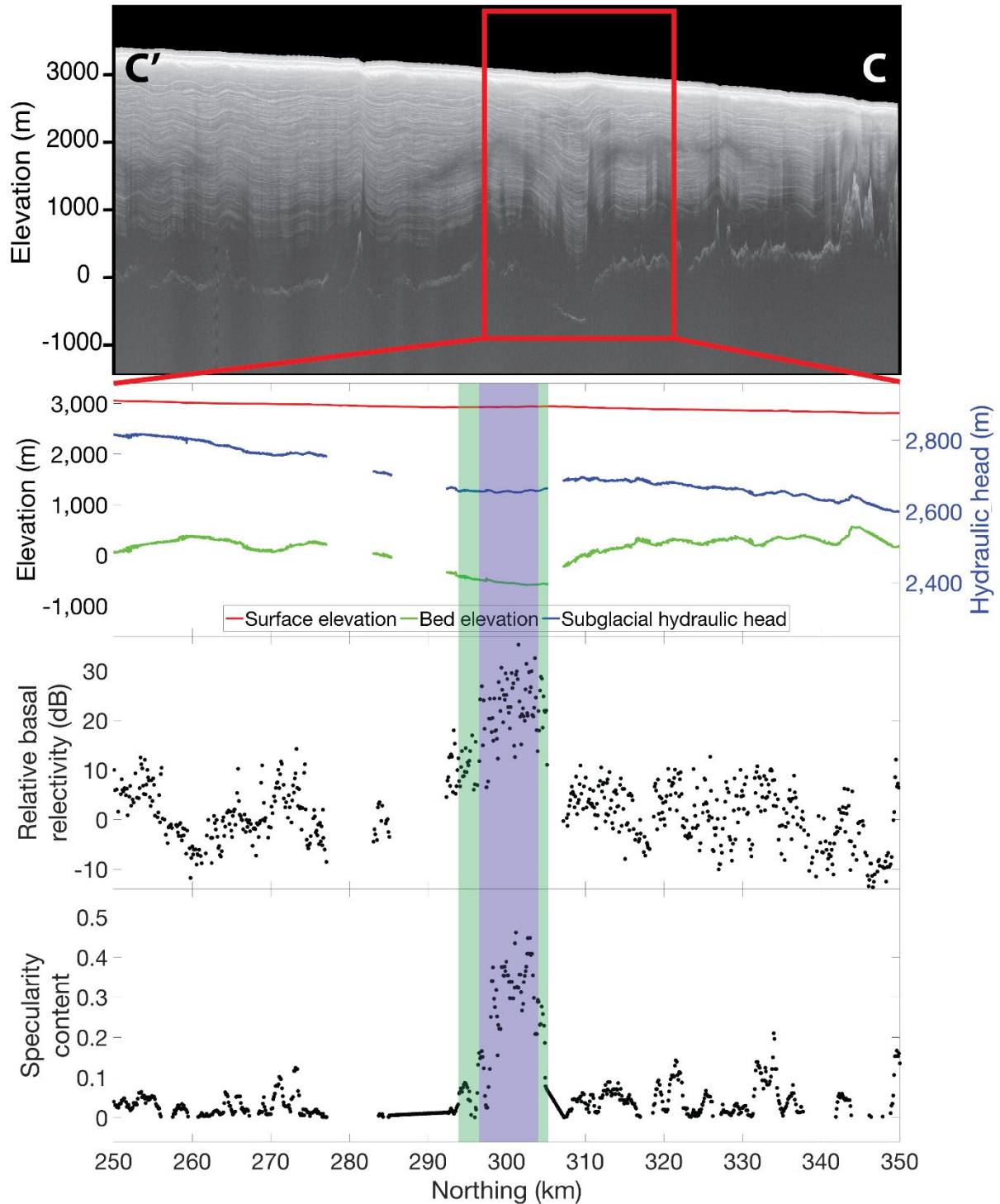
Supplementary Figure 2. Ice sheet geometry, subglacial hydraulic head, relative basal reflectivity, and basal specularity content derived from ice-penetrating radar profile LSE/JKB2u/X59a. Location and orientation of the profile are illustrated in Supplementary Fig. 1. The blue rectangle marks the interpreted lake area. The green rectangle marks the interpreted sediment area.

LSE/GCX0f/X61a



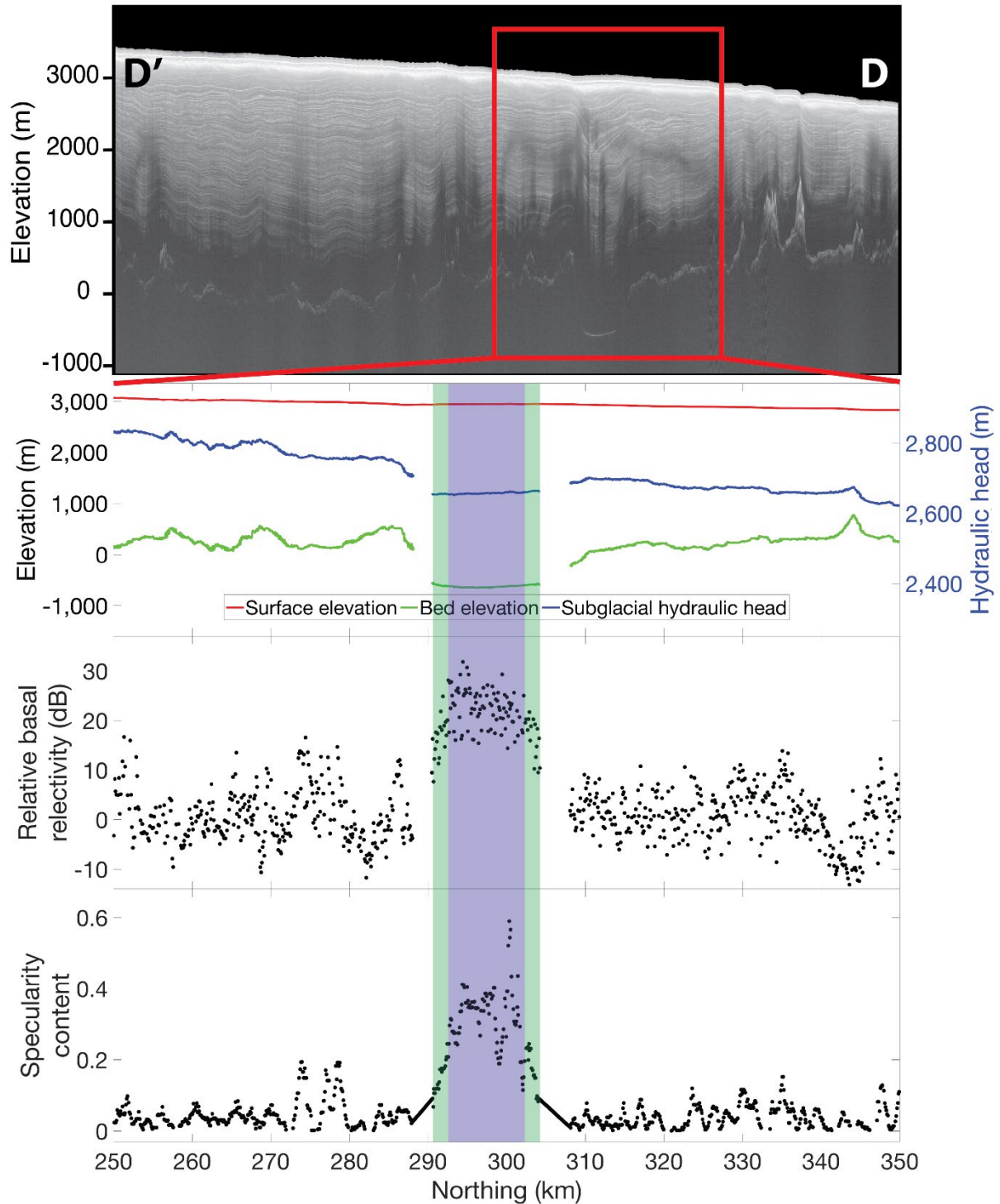
Supplementary Figure 3. Ice sheet geometry, subglacial hydraulic head, relative basal reflectivity, and basal specularity content derived from ice-penetrating radar profile LSE/GCX0f/X61a. Location and orientation of the profile are illustrated in Supplementary Figure 1. The blue rectangle marks the interpreted lake area. The green rectangle marks the interpreted sediment area.

LSE/GCX0e/Y81a



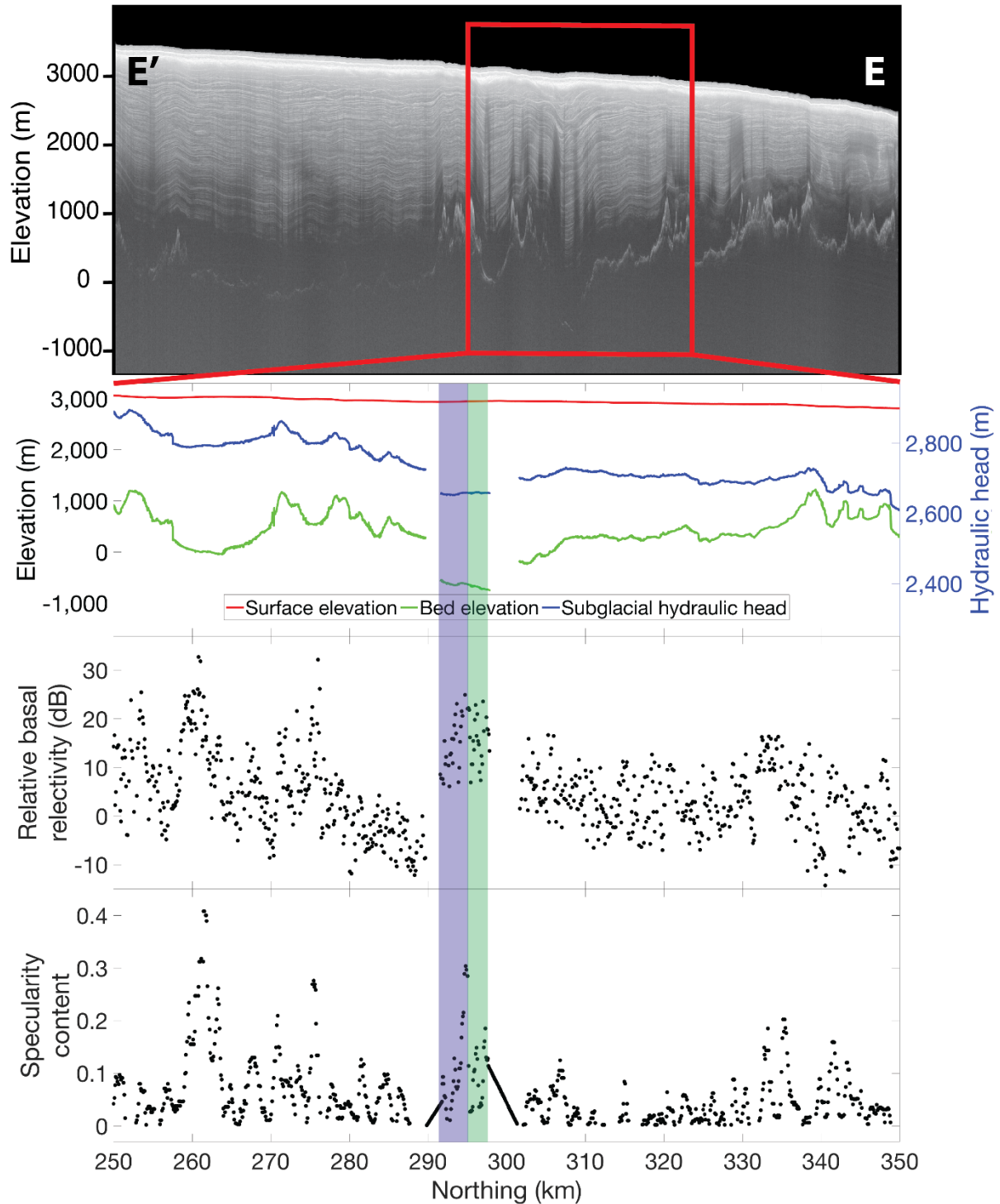
Supplementary Figure 4. Ice sheet geometry, subglacial hydraulic head, relative basal reflectivity, and basal specularity content derived from ice-penetrating radar profile LSE/GCX0e/Y81a. Location and orientation of the profile are illustrated in Supplementary Figure 1. The blue rectangle marks the interpreted lake area. The green rectangle marks the interpreted sediment area.

LSE/GCX0e/Y87a

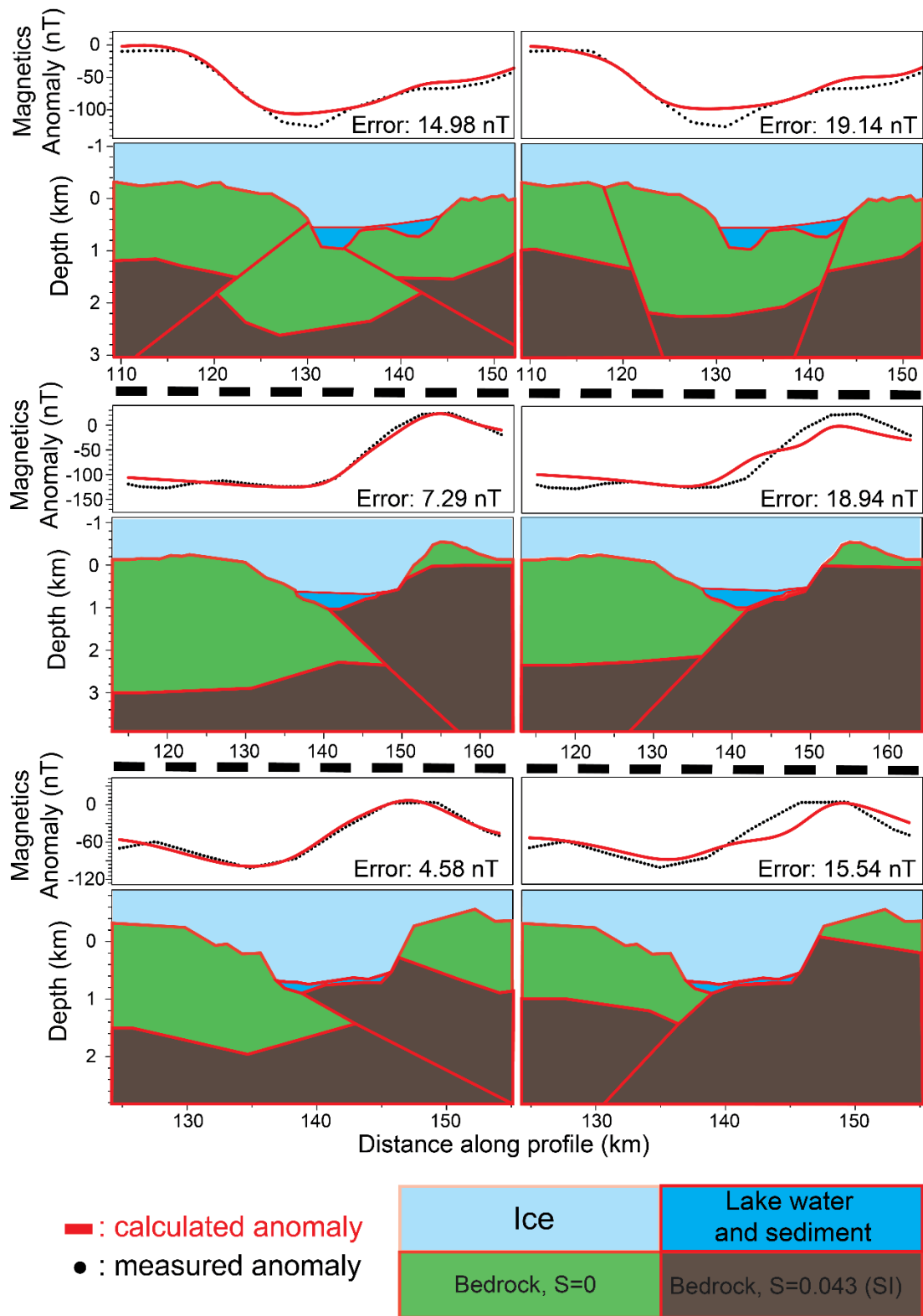


Supplementary Figure 5. Ice sheet geometry, subglacial hydraulic head, relative basal reflectivity, and basal specularity content derived from ice-penetrating radar profile LSE/GCX0e/Y87a. Location and orientation of the profile are illustrated in Supplementary Figure 1. The blue rectangle marks the interpreted lake area. The green rectangle marks the interpreted sediment area.

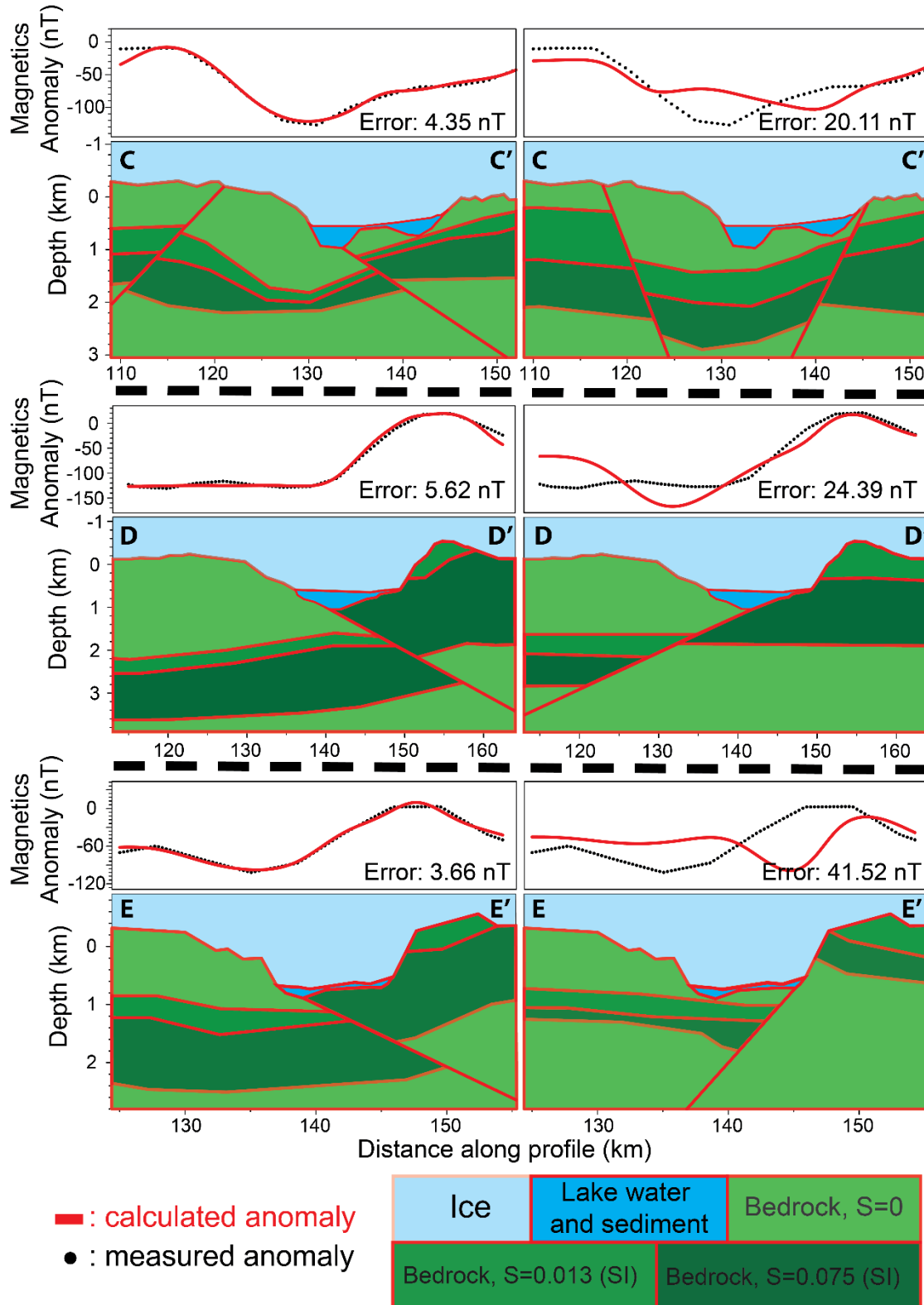
LSE/GCX0e/Y93a



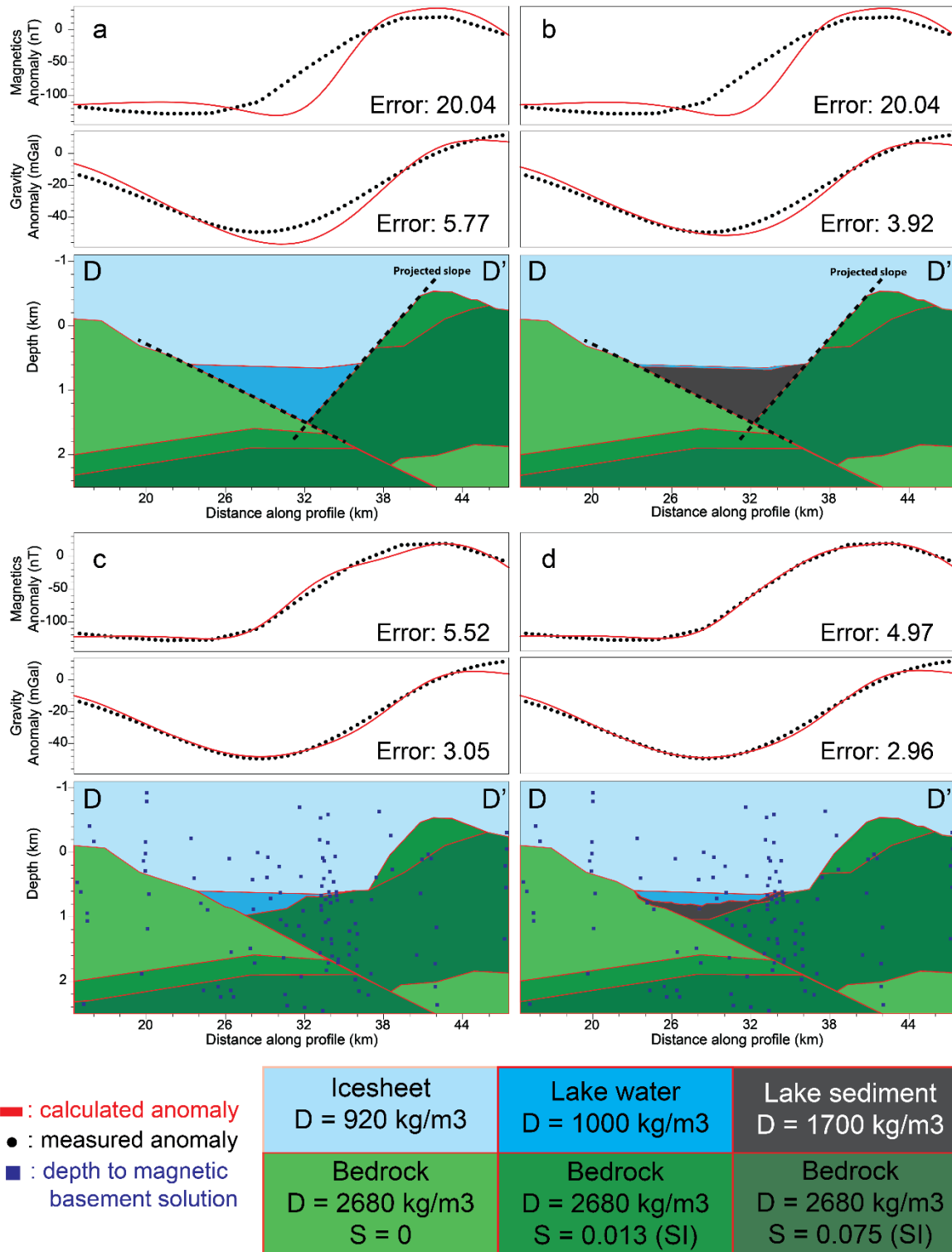
Supplementary Figure 6. Ice sheet geometry, subglacial hydraulic head, relative basal reflectivity, and basal specularity content derived from ice-penetrating radar profile LSE/GCX0e/Y93a. Location and orientation of the profile are illustrated in Supplementary Figure 1. The blue rectangle marks the interpreted lake area. The green rectangle marks the interpreted sediment area.



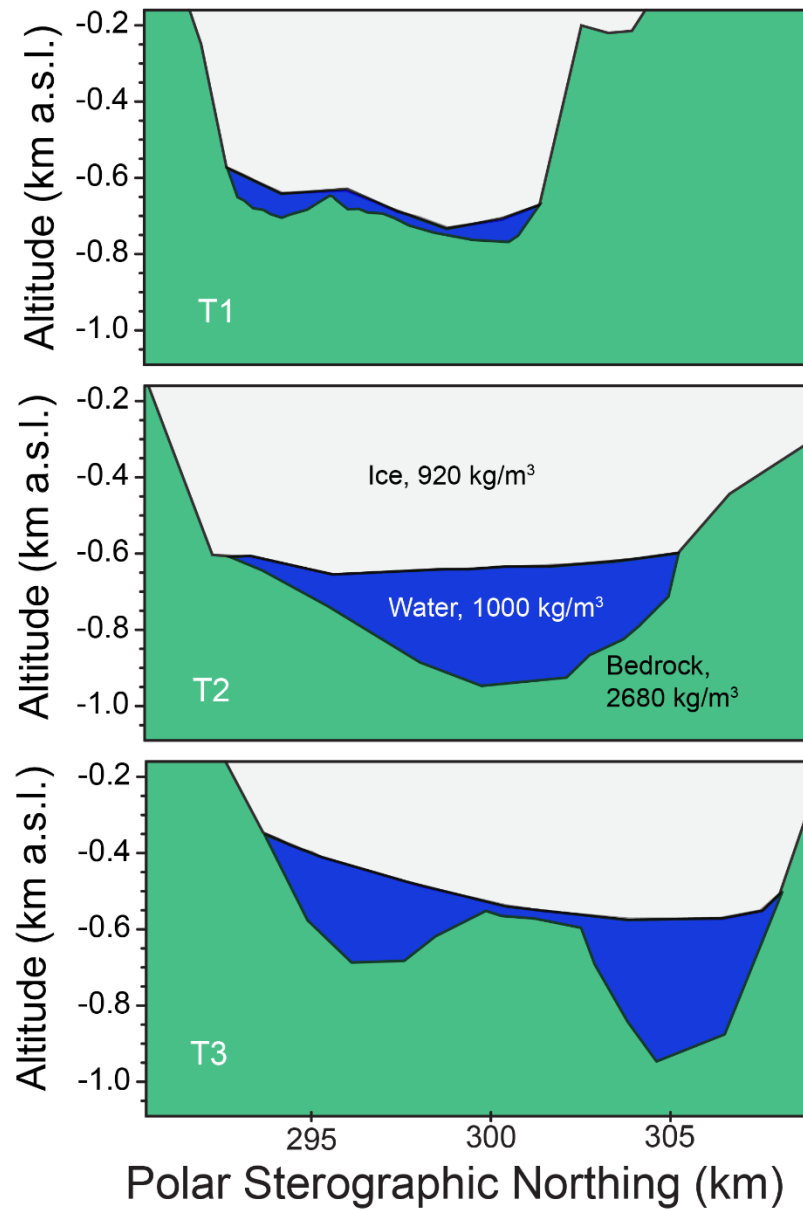
Supplementary Figure 7. Modeled magnetic response of different geological models compared to the measured signals along three profiles across LSE. Locations and orientations of the profiles are illustrated in Supplementary Figure 1.



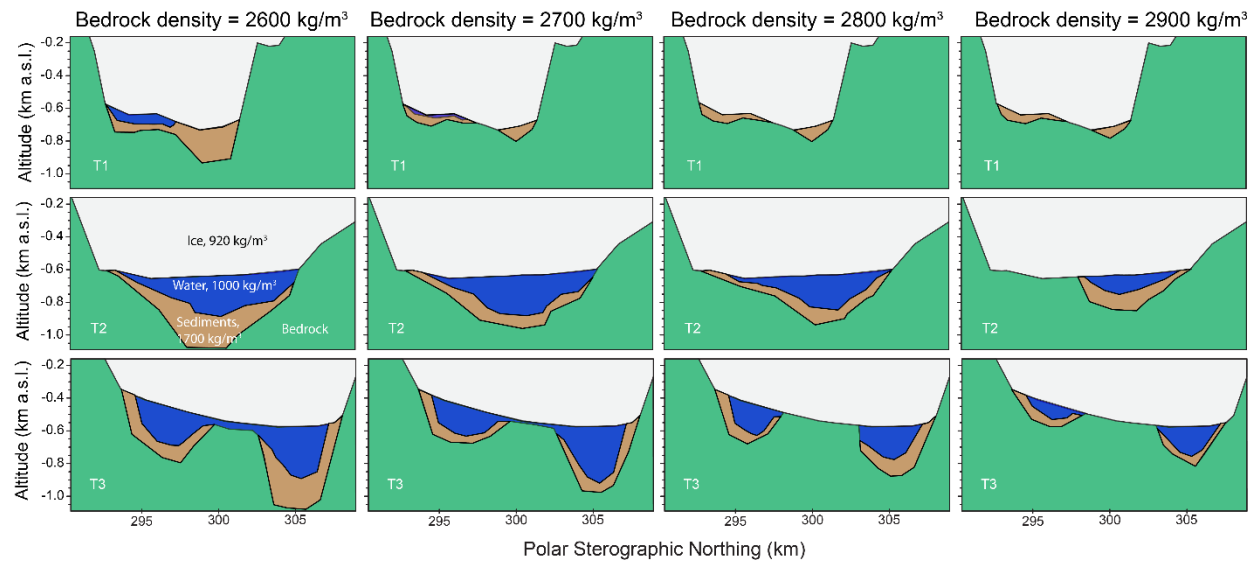
Supplementary Figure 8. Modeled magnetic response of different geological models compared to the measured signals along three profiles across LSE. Locations and orientations of the profiles are illustrated in Supplementary Figure 1.



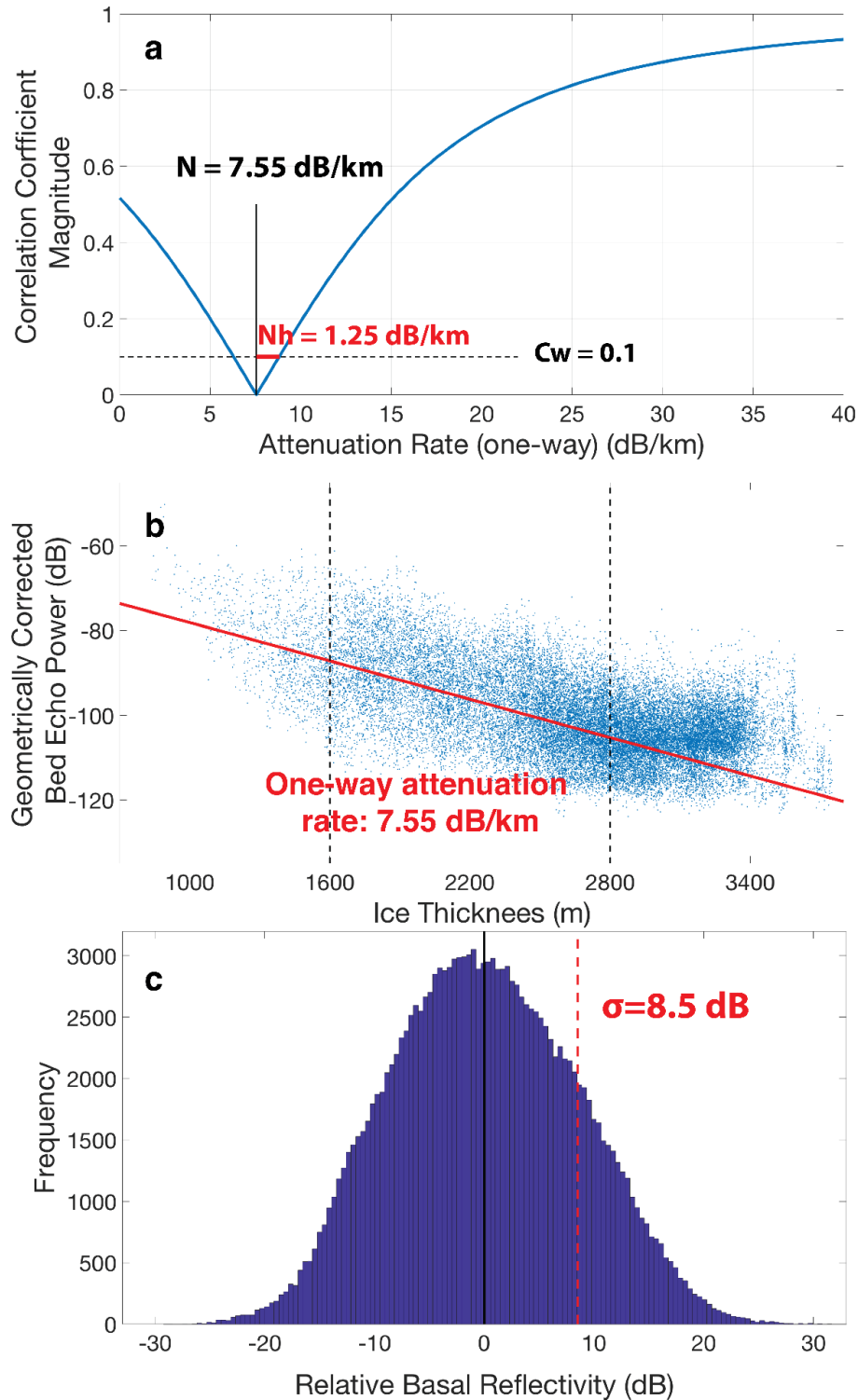
Supplementary Figure 9. Modeled magnetic and gravity response of four different bathymetry models along profile D-D' compared to the measured signals. Location and orientation of the profile are illustrated in Supplementary Figure 1.



Supplementary Figure 10. Gravity inversion of the water depth with no sediment. Location of the profiles are illustrated in Figure 3.



Supplementary Figure 11. Gravity inversion of the water and sediment thickness with a range of bedrock densities. Location of the profiles are illustrated in Figure 3.



Supplementary Figure 12. Estimation of the radar attenuation rate. a, A global one-way attenuation rate of 7.55 dB/km is estimated by the minimum correlation coefficient magnitude method. The attenuation rate uncertainty N_h is estimated to be 1.25 dB/km . b, Linear regression between measured ice thickness and geometrically corrected bed echo power from radio-echo sounding. c, Histogram of derived relative basal reflectivity.